

1 **Surface and subsurface dynamics of a perennial slow-moving landslide from**  
2 **ground, air and space**

3 Xie Hu<sup>1\*</sup>, Roland Bürgmann<sup>1</sup>, William H. Schulz<sup>2</sup>, and Eric J. Fielding<sup>3</sup>

4  
5 <sup>1</sup>Department of Earth and Planetary Science, University of California, Berkeley, California,  
6 USA

7 <sup>2</sup>U.S. Geological Survey, Denver, CO, USA

8 <sup>3</sup>Jet Propulsion Laboratory, California Institute of Technology, Pasadena, CA, USA

9 Correspondence to: xiehu@berkeley.edu  
10

11 **Landslides modify the natural landscape and cause fatalities and property damage**  
12 **worldwide. Quantifying landslide dynamics is challenging due to the stochastic nature of**  
13 **the environment. With its large area of ~1 km<sup>2</sup> and perennial motions at ~10-20 mm/day,**  
14 **the Slumgullion landslide in Colorado, USA represents an ideal natural laboratory to**  
15 **better understand landslide behavior. Here we use hybrid remote sensing data and**  
16 **methods to recover the four-dimensional surface motions during 2011-2018. We resolve a**  
17 **new mobile area of ~0.35 km<sup>2</sup> below the crest of the prehistoric landslide. We construct a**  
18 **mechanical framework to quantify the rheology, subsurface channel geometry, mass flow**  
19 **rate, and spatiotemporally dependent pore-water pressure feedback through a joint**  
20 **analysis of displacement and hydrometeorological measurements from ground, air and**  
21 **space. Variations in recharge, mainly from snowmelt, drive multi-annual decelerations and**  
22 **accelerations, during which the head of the landslide is the most responsive. Our study**  
23 **demonstrates the importance of remotely characterizing often inaccessible, dangerous**  
24 **slopes to better understand landslide mechanisms, landscape modification, and other**  
25 **quasi-static mass fluxes in natural and industrial environments, and will ultimately help**  
26 **reduce landslide hazards.**

27 Landslides denude mountains, transport sediments to rivers, lakes and oceans, and modify the  
28 Earth's surface environment and ecosystem. Landslides of all sizes and rates represent  
29 geohazards that may lead to property damage and casualties. The hazards that landslides present  
30 and their impact on Earth's surface primarily depend on their volume and the rate at which they  
31 move, as well as their responsiveness to hydroclimatic variability. However, quantifying  
32 landslide dynamics is challenging due to the stochastic nature of the environment (e.g., geology,  
33 geomorphology, vegetation), external disturbances (e.g., fire, climate change, earthquakes,  
34 logging), and the limited availability of observations (e.g., remote, surface and subsurface  
35 geodetic, geophysical and hydrological measurements)<sup>1-5</sup>. Knowledge of landslide behavior  
36 primarily depends on isolated measurements made on and within the landslides, which are often  
37 cost prohibitive or even impossible to obtain, and their value is limited by conservative  
38 interpretations for generalizing to the entirety of dynamically complex landslides. Incomplete  
39 information of three-dimensional (3D) surface displacements has limited our ability to infer the  
40 continuous landslide depth, interpret the driving and resisting mechanisms, and develop accurate  
41 forecasts for landslides. Here we compile a comprehensive dataset of remote sensing imagery  
42 from air and space, meteorological records, and in-situ surface (extensometer) and subsurface  
43 (inclinometer) deformation measurements, allowing us to develop a systematic framework for  
44 using detailed, temporally-variable 3D surface deformation data to quantify the underlying  
45 landslide kinematics and dynamics.

46

47 For centuries, the Slumgullion landslide in the San Juan Mountains of Colorado has snaked its  
48 way downhill at  $\sim 10\text{-}20\text{ mm/day}^{5-16}$ , allowing us to explore both transient and quasi steady-state  
49 mass wasting processes. The original 700-year-old failure initiated from the edge of the Cannibal

50 Plateau, formed Lake San Cristobal, and is currently inactive (Fig. 1). About 300 years ago, an  
51 approximately 3,900-m-long and 150- to 450-m-wide section of the landslide reactivated from  
52 the original headscarp to a new toe above Highway 149. The landslide deposits consist of  
53 hydrothermally altered Tertiary volcanic rocks.

54  
55 Interferometric Synthetic Aperture Radar (InSAR) has been widely used to measure ground  
56 motions for geohazards research<sup>17-19</sup>, but its application at Slumgullion is challenged by high  
57 deformation gradients. Additionally, the reconstruction of 3D surface displacements depends on  
58 the availability of multiple view angles and their distribution<sup>16, 20</sup>. Here we incorporate data from  
59 the ascending and descending tracks of Copernicus spaceborne C-band Sentinel-1 SAR (2017-  
60 2018) and four flight lines of the NASA/JPL airborne L-band Uninhabited Aerial Vehicle SAR  
61 (UAVSAR) (2011-2018; Fig. 1A) with a hybrid InSAR phase and SAR amplitude pixel offset  
62 tracking (POT) time-series analysis (Figs. S1-S2; Table S1)<sup>21-22</sup>. The advance in data and method  
63 integration illuminates the spatiotemporal 3D surface evolution from 1000+ individual  
64 displacement maps (Figs. S3-S4), two orders of magnitude more than previous SAR-based  
65 studies<sup>14-16</sup>.

## 66 67 **Results**

### 68 **Spatial displacement patterns**

69 The 98-scenes of Sentinel-1 SAR reveal displacement details over the more slowly deforming  
70 head and toe areas of the landslide (Fig. 1B-C). The fast-moving middle parts are not resolvable  
71 due to extreme InSAR phase gradients at the available Sentinel-1 orbital period, radar  
72 wavelength, and the amount of displacement over a short distance (see Methods). We recognize

73 a new kinematic element in an area of  $\sim 0.35 \text{ km}^2$  below the crest of the prehistoric landslide  
74 (Fig. 1A), which accounts for  $\sim 1/3^{\text{rd}}$  of the previously mapped mobile area<sup>8-9, 14</sup>. We further  
75 update the structural zones<sup>9</sup>: head zone (kinematic elements #1-3) exposed by extensional  
76 fractures, zone of stretching (#4-6) characterized by broad bands of tension cracks and normal  
77 faults, hopper & neck (#7-8) resembling a funnel, zone of marginal pull-apart basins (#9-10)  
78 accompanying widening of the slide, and toe (#11-12) overriding inactive surfaces. The current  
79 major source of debris supply appears to be on the upper flank of the head (blackish area in Fig.  
80 1B-C with motion to east). Here, the sediments are transported along a curved track parallel to  
81 the margin between elements 1 and 2, at a large angle from the main stream of the slide.

82

83 To systematically analyze the kinematics and mechanics of Slumgullion, we rely on 3D velocity  
84 fields that describe the steady state, slow-moving earth flow. We obtain eight velocity  
85 measurements from four UAVSAR flight lines during each sortie in their respective azimuth and  
86 range directions. The hybrid InSAR-POT analysis provides us a robust 3D solution over the  
87 entire active landslide area, with a total of 124 scenes. We represent the deformation in a series  
88 of 77 transverse profiles (Figs. 2A and S5). The displacements in the steep upper head zone are  
89 highly variable with low signal-to-noise ratio (SNR). Velocity measurements become more  
90 coherent from the intersection between the head and the zone of stretching, moving at about 2.5  
91 mm/day. The south part of the zone of stretching moves at 7 mm/day, and elongated flank ridges  
92 extend along its southeastern lateral margin (Fig. S5). The movement rotates westerly to the  
93 narrow hopper & neck. The velocity profiles regain a symmetric pattern with rates as high as 13  
94 mm/day at the center. The surface topography gradually develops a bump along the central axis  
95 (Fig. S5). The rates decrease to  $\leq 10$  mm/day in the zone of marginal pull-apart basins, and the

96 velocity profiles appear asymmetric around the internal bends. An oversteepened northwest-  
97 facing slope divides the toe, and the southern part moves faster along this internal right-lateral  
98 fault at up to 6 mm/day. The persistently advancing landslide toe results in shifted fronts with  
99 respect to those mapped in the summer of 1991<sup>8</sup>. Multiple pieces of evidence validate the  
100 advance of the toe over its substrate. UAVSAR-derived 2011-2018 horizontal velocities at the tip  
101 of the toe reach 4-5 mm/day, consistent with the rate determined from aerial photos taken in  
102 1985 and 1990 (ref. 9). The mapped shifts (Fig. 3) and the topographic back-projection (Fig. S6)  
103 also show that the toe has advanced by ~40 m during the past two decades.

104

#### 105 **Inferred landslide channels and subsurface flow**

106 The transverse longitudinal velocities allow us to invoke the depth-integrated law of mass  
107 conservation in order to estimate the local free-surface height from the slide channel bottom.  
108 Viscoplastic flow models suggest that the longitudinal shear velocities at the surface mirror the  
109 shape of the subsurface channel<sup>23, 24</sup>. We propose a novel geometric description of the landslide  
110 channel, which characterizes the depth, the steepness between the basal bed surface and the  
111 lateral margins, and the tilt of the basal bed across the landslide with respect to the horizontal  
112 (Figs. 2 and S7-S10). We use the longitudinal surface-velocity profiles to invert for these  
113 geometric parameters. The largest depth (<~30 m) is inferred underneath the fastest-moving  
114 hopper & neck. High steepness values concentrate at the zone of marginal pull-apart basins in the  
115 lower part of the slide. According to the inferred degree of bed tilting, the head and toe areas are  
116 more asymmetric, consistent with their irregular outlines. The bed starts from a minor NW tilt in  
117 the zone of stretching and transitions to the largest positive SE tilt at the biggest bend of the

118 slide. Our quantification of the landslide geometry yields a total volume of  $1.33 \times 10^7 \text{ m}^3$ ,  
119 compared to a previous estimate of  $1.95 \times 10^7 \text{ m}^3$  (ref. 8).

120

121 We can also resolve the subsurface viscoplastic flow rate along with the channel geometry (Fig.  
122 2C-E). Insignificant shear deformation down to about 10-m depth found at the borehole  
123 inclinometer indicates that the landslide materials are highly plastic and follow non-Newtonian  
124 behavior (Fig. S11). Additionally, SAR and extensometer measurements at lateral flanks reveal  
125 appreciable highly localized deformation that suggests a pseudo-plastic rheology at shallow  
126 depths. Therefore, we apply the power-law flow theory to characterize the upper pseudo-plug  
127 and the lower yield zone above the underlying bedrock<sup>25</sup> (see Methods). We can quantify the  
128 power-law index as 0.7 and the consistency index as  $1.34 \times 10^{10} \text{ Pa} \cdot \text{s}^n$  based on the inferred  
129 landslide thickness at the distal toe (Fig. S12; Table S2). High velocity gradients concentrate  
130 near the bottom of the slide and approach 0 at shallower depths (Fig. 2C).

131

### 132 **Hydrological forcing and time-dependent landslide deformation**

133 We also explore the landslide behavior controlled by the time-variant hydrological environment.  
134 As fluid water is the essential agent that regulates the pore pressure<sup>1, 26-27</sup>, we explicitly consider  
135 the forms of precipitation and determine the daily fluid water from snowmelt and rainwater (see  
136 Methods). The water year 2018 (10/1/2017-9/30/2018) was historically dry with only 64% of  
137 1981-2010 precipitation average. There was another dry water year in 2013 from the estimated  
138 fluid water recharge, however this is barely discernible from raw precipitation data (Fig. 4B and  
139 Fig. S13). From the recharge time series we simulate pore pressures at depth as a one-  
140 dimensional diffusive process from the surface (see Methods; Fig. S14).

141  
142 We investigate the slide's temporal response to the estimated seasonal and multi-annual fluid  
143 water changes by comparing Sentinel-1 InSAR results of August in 2017 (wet) and 2018 (dry),  
144 for which time-series solutions are available for both tracks (Fig. 4A). Between the two time  
145 periods, radar line-of-sight (LOS) rates slowed down by 90% at high elevations (3450 m), the  
146 rate reduction decreases linearly to 70% over the upper slide (3300 m elevation), while it is only  
147 around 45% in the toe area (2950-3100 m elevation). Extensometers located on the southern  
148 flanks of elements 6, 10 and 12 show decelerations by 66%, 40% and 49%, respectively,  
149 between the same periods (Fig. 3B). The variable rate decreases in response to the reduced water  
150 recharge imply spatiotemporal diversity of pore pressure feedback.

151  
152 The UAVSAR hybrid InSAR and POT analysis captures the temporal behavior of the whole  
153 landslide during 2011-2018 at a coarser temporal sampling (Fig. 4B; Figs. S15-S16). The time  
154 series of downslope motions from UAVSAR and three extensometers match well (Fig. 3B).  
155 Based on the long-term changes in the fluid-water recharge history, we consider three multi-  
156 annual phases of 08/2011-11/2013, 04/2013-11/2017, and 10/2016-10/2018. We use an  
157 exponential model to quantify the multi-annual rate changes (i.e., the velocity changes with  
158 respect to initial conditions for each period, see Methods). Element 1 was excluded due to small  
159 SNR. Agreeing well with the hydrological processes, the inferred rate changes are negative for  
160 2011-2013 and 2016-2018, indicative of slowing down, contrasting with the inferred speeding up  
161 during 2013-2017 (Figs. 4 and S17-S18). The head area consistently responds most sensitively to  
162 recharge changes during all three phases (Fig. 4C).

163

164 The distribution of UAVSAR-measured rate changes with position on the landslide is consistent  
165 with the deceleration vs. elevation/position relationship observed during 2017-2018 with  
166 Sentinel-1, as well as the extensometer data. This suggests a correlation between the landslide  
167 depth and sensitivity to hydrological forcing. This is physically consistent because the diffusive  
168 pore pressure changes more strongly and rapidly at shallow depths, while the response is  
169 increasingly damped and delayed at greater depths. For example, the onset of the pore-pressure  
170 increase at 20-m depth lags behind that at 10-m depth by ~12 days according to the constrained  
171 diffusion model adjusted by the average pore pressure measured previously<sup>12</sup> of 177 kPa (Fig.  
172 S14).

173

#### 174 **Implications for the perennial motions of landslides**

175 Water recharge at the Slumgullion increases twice per year, from snowmelt in late spring and  
176 rainfall in early fall, which results in a more stable nearly saturated system than landslides that  
177 experience only one significant annual recharge episode. For instance, the near-saturation  
178 condition can last for about half time of the year from March at a characteristic depth of 20 m  
179 (Fig. S14). Our results also show that over time scales of several years, the Slumgullion  
180 accelerates and decelerates due to multi-year hydrological fluctuations, supporting the hypothesis  
181 that it and other landslides in the Rocky Mountains will slow in future decades due to predicted  
182 temperature increases, precipitation decreases, and a depletion of supply<sup>13</sup>. Other factors, such as  
183 changes in vegetation cover and possible large failures at the headscarp, could make the situation  
184 more complicated<sup>13</sup>. Moreover, other stabilizing mechanisms, such as shear strength that  
185 increases with shear displacement rate, shear-induced dilative strengthening, soil wetting and  
186 swelling along the lateral margins above the water table, and the forced circulation of pore fluid



187 around asperities may help augment the resistance<sup>27-30</sup>. Hourly sampled subsurface strain and  
188 pore pressure data and laboratory testing may be able to identify and distinguish these  
189 contributions to the landslide strength. If such forces play a role, we can qualitatively determine  
190 that the landslide neck with large contact areas along the sides, and the zones of hopper & neck  
191 and pull-apart basins that have large irregularities in landslide depth and steepness, may provide  
192 additional stabilizing force.

193  
194 Unprecedented, interdisciplinary observations, methods and models combined help to advance  
195 the characterization of landslide dynamics. Remotely sensed SAR data and hybrid processing  
196 methods allow us to achieve 3D spatiotemporal surface displacements. In-situ datasets such as  
197 the extensometer measurements validate and calibrate the SAR results from air and space; the  
198 inclinometer data provide evidence on the non-Newtonian behavior of the landslide mass,  
199 together with the SAR/extensometer-confirmed mobility at the margins, support the application  
200 of power-law viscoplastic flow theory; the precipitation and temperature records illuminate the  
201 fluid recharge from snowmelt and rainwater; the piezometer-measured average pore pressures  
202 help translate recharge at the surface to pore pressures at depth. Our study sheds new light on the  
203 landslide boundaries, geometry, subsurface flow, and how different structural zones respond to  
204 the hydroclimatic variability. Beyond that, our systematic chains of analysis can also be applied  
205 in full or in part to help understand other quasi-static viscoplastic flow processes associated with  
206 solid particles with an interstitial fluid, such as debris slides, volcanic lahars, and submarine  
207 slides.

208 **References:**

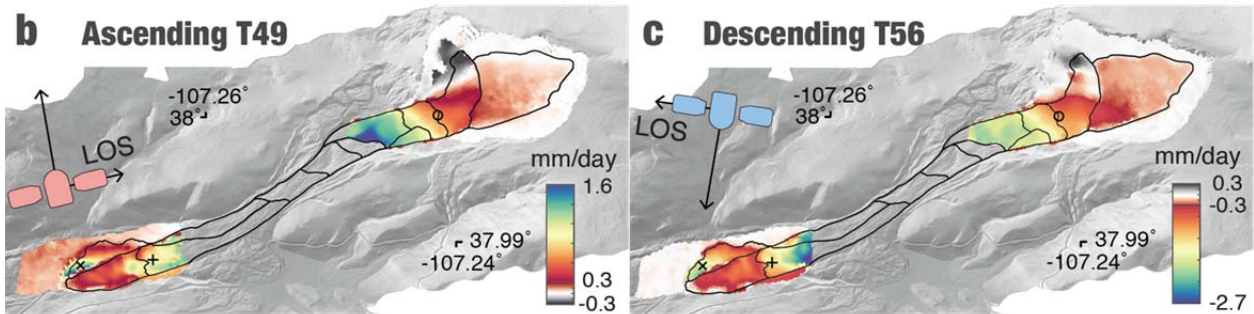
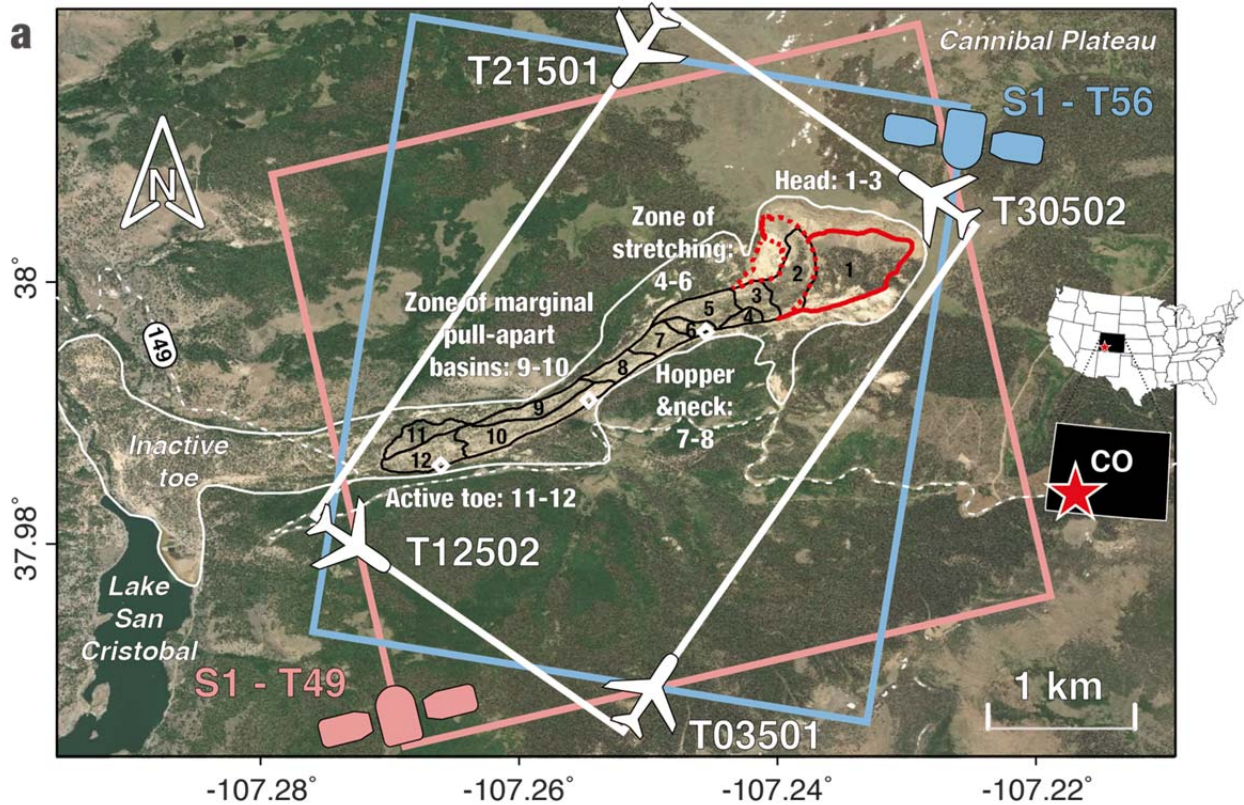
- 209 1. Iverson, R. M. & LaHusen, R. G. Dynamic pore-pressure fluctuations in rapidly shearing  
210 granular materials. *Science* **246**, 796–799 (1989).
- 211 2. Schulz, W. H., Kean, J. W. & Wang, G. Landslide movement in Southwest Colorado  
212 triggered by atmospheric tides. *Nat. Geosci.* **2**, 863–866 (2009).
- 213 3. Roering, J. J., Mackey, B. H., Handwerger, A. L., Booth, A. M., Schmidt, D. A., Bennett, G.  
214 L. & Cerovski-Darriau, C. Beyond the angle of repose: A review and synthesis of landslide  
215 processes in response to rapid uplift, Eel River, Northern California. *Geomorphology* **236**,  
216 109–131 (2015).
- 217 4. Kargel, J. S., et al. Geomorphic and geologic controls of geohazards induced by Nepal’s  
218 2015 Gorkha earthquake. *Science* **351**, aac8353 (2016).
- 219 5. Palmer, J. Creeping earth could hold secret to deadly landslides. *Nature* **548**, 384–386 (2017).
- 220 6. Howe, E. Landslides in the San Juan Mountains, Colorado. *US Geol. Surv. Professional*  
221 *Paper* 67 (US Geological Survey, 1909).
- 222 7. Crandell, D. R. & Varnes, D. J. Movement of the Slumgullion earthflow near Lake City,  
223 Colorado. *US Geol. Surv. Professional Paper* 424-B (US Geological Survey, 1961).
- 224 8. Parise, M. & Guzzi, R. Volume and shape of the active and inactive parts of the Slumgullion  
225 landslide, Hinsdale County, Colorado. *US Geol. Surv. Open-File Report* 92-216 (US  
226 Geological Survey, 1992).
- 227 9. Fleming, R. W., Baum, R. L. & Giardino, M. Map and description of the active part of the  
228 Slumgullion landslide, Hinsdale County, Colorado. *US Geol. Surv. Geol. Inv. Ser. Map* I-  
229 2672 (U.S. Geological Survey, 1999).

- 230 10. Coe, J. A., Ellis, W. L., Godt, J. W., Savage, W. Z., Savage, J. E., Michael, J. A., et al.  
231 Seasonal movement of the Slumgullion landslide determined from Global Positioning  
232 System surveys and field instrumentation, July 1998–March 2002. *Eng. Geol.* **68**, 67–101  
233 (2003).
- 234 11. Coe, J. A., Mckenna, J. P., Godt, J. W. & Baum, R. L. Basal-topographic control of  
235 stationary ponds on a continuously moving landslide. *Earth Surf. Proc. Land.* **34**, 264–279  
236 (2009).
- 237 12. Schulz, W. H., Mckenna, J. P., Kibler, J. D. & Biavati, G. Relations between hydrology and  
238 velocity of a continuously moving landslide—Evidence of pore-pressure feedback regulating  
239 landslide motion? *Landslides* **6**, 181–190 (2009).
- 240 13. Coe, J. A. Regional moisture balance control of landslide motion: Implications for landslide  
241 forecasting in a changing climate. *Geology* **40**, 323–326 (2012).
- 242 14. Schulz, W. H., Coe, J. A., Ricci, P. P., Smoczyk, G. M., Shurtleff, B. L. & Panosky, J.  
243 Landslide kinematics and their potential controls from hourly to decadal timescales: Insights  
244 from integrating ground-based InSAR measurements with structural maps and long-term  
245 monitoring data. *Geomorphology* **285**, 121–136 (2017).
- 246 15. Milillo, P., Fielding, E. J., Schulz, W. H., Delbridge, B. G. & Bürgmann, R. COSMO-  
247 SkyMed spotlight interferometry over rural areas: The Slumgullion landslide in Colorado,  
248 USA. *IEEE J. Sel. Topics Appl. Earth Observ. Remote Sens.* **7**, 2919–2926 (2014).
- 249 16. Delbridge, B. G., Bürgmann, R., Fielding, E. J., Hensley, S. & Schulz, W. H. 3D surface  
250 deformation derived from airborne interferometric UAVSAR: Application to the Slumgullion  
251 landslide. *J. Geophys. Res.* **121**, 3951–3977 (2016).

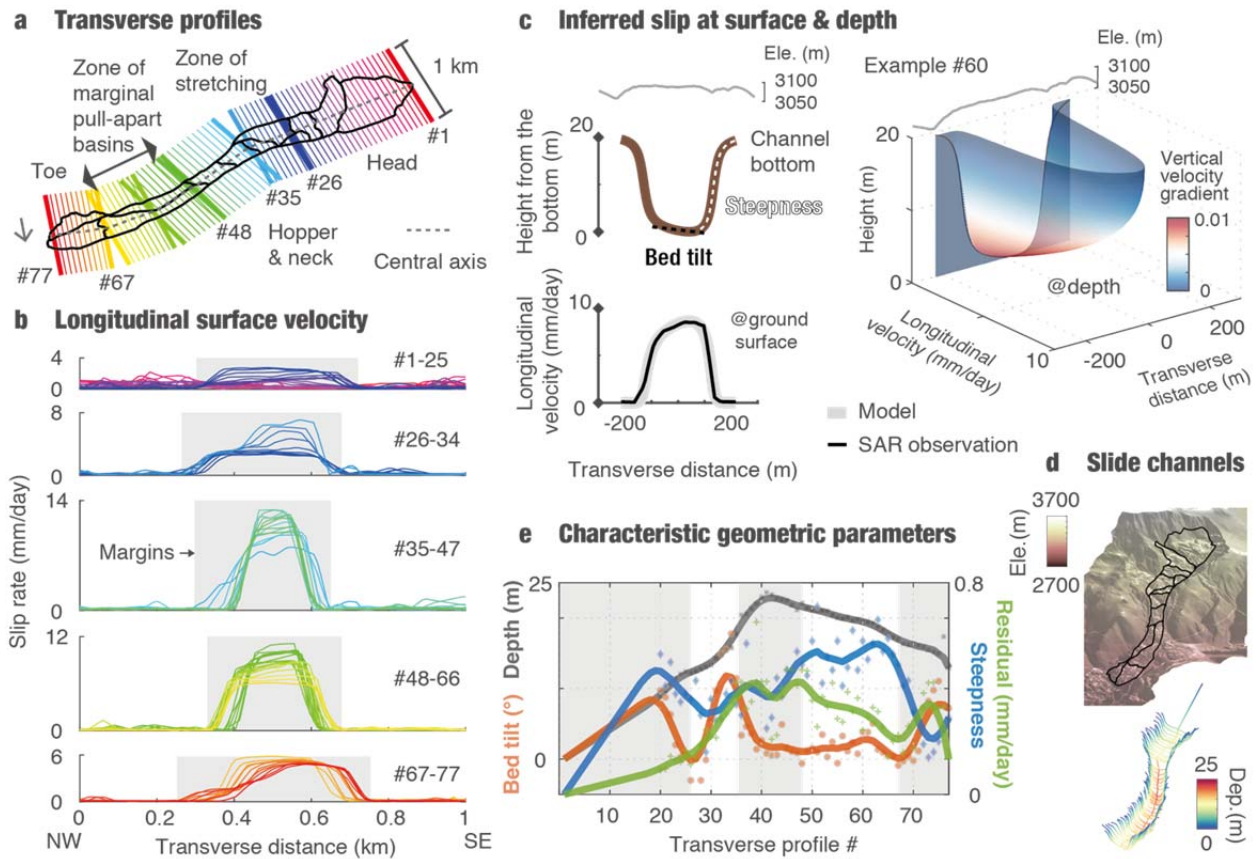
- 252 17. Bürgmann, R., Rosen, P. A. & Fielding, E. J. Synthetic aperture radar interferometry to  
253 measure Earth's surface topography and its deformation. *Annual Rev. Earth Planet. Sci.* **28**,  
254 169–209 (2000).
- 255 18. Hilley, G. E., Bürgmann, R., Ferretti, A., Novali, F. & Rocca, F. Dynamics of slow-moving  
256 landslides from permanent scatterer analysis. *Science* **304**, 1952–1955 (2004).
- 257 19. Hu, X., Lu, Z., Pierson, T. C., Kramer, R. & George, D. L. Combining InSAR and GPS to  
258 determine transient movement and thickness of a seasonally active low- $\alpha$  gradient  
259 translational landslide. *Geophysical Res. Lett.* **45**, 1453–1462 (2018).
- 260 20. Hu, X., Bürgmann, R., Lu, Z., Handwerger, A. L., Wang, T. & Miao, R. Mobility, thickness,  
261 and hydraulic diffusivity of the slow-moving Monroe landslide in California revealed by L-  
262 band satellite radar interferometry. *J. Geophys. Res.* **124** (2019).
- 263 21. Hensley, S., Wheeler, K., Sadowy, G., Miller, T., Shaffer, S., Muellerschoen, R., Jones, C.,  
264 Zebker, H., Madsen, S. & Rosen, P. Status of a UAVSAR designed for repeat pass  
265 interferometry for deformation measurements. *IEEE MTT-S International Microwave*  
266 *Symposium* **3**, 1453-1456 (2005).
- 267 22. Hu, X., Wang, T. & Liao, M. Measuring coseismic displacements with point-like targets  
268 offset tracking. *IEEE Geosci. Remote Sens. Lett.* **11**, 283-287 (2014).
- 269 23. Mei, C. C. & Yuhi, M. Slow flow of a Bingham fluid in a shallow channel of finite width. *J.*  
270 *Fluid Mech.* **431**, 135–159 (2001).
- 271 24. van Asch, T. W. J., Van Beek, L. P. H. & Bogaard, T. A. Problems in predicting the mobility  
272 of slow-moving landslides. *Eng. Geol.* **91**, 46-55 (2007).

- 273 25. Longo, S., Di Federico, V. & Chiapponi, L. Propagation of viscous gravity currents inside  
274 confining boundaries: the effects of fluid rheology and channel geometry. *Proc. R. Soc. A*  
275 **471** (2015).
- 276 26. Cohen-Waeber, J., Bürgmann, R., Chaussard, E., Giannico, C. & Ferretti, A. Spatiotemporal  
277 patterns of precipitation-modulated landslide deformation from independent component  
278 analysis of InSAR time series. *Geophys. Res. Lett.* **45** (2018).
- 279 27. Handwerger, A. L., Fielding, E. J., Huang, M.-H., Bennett, G. L., Liang, C. & Schulz, W. H.  
280 Widespread initiation, reactivation, and acceleration of landslides in the northern California  
281 Coast Ranges due to extreme rainfall. *J. Geophys. Res.* **124**, 1782–1797 (2019).
- 282 28. Iverson, R. M., Reid, M. E., Iverson, N. R., LaHusen, R. G., Logan, M., Mann, J. E. & Brien,  
283 D. L. Acute sensitivity of landslide rates to initial soil porosity. *Science* **290**, 513–516 (2000).
- 284 29. Schulz, W. H., Smith, J. B., Wang, G., Jiang, Y. & Roering, J. J. Clayey landslide initiation  
285 and acceleration strongly modulated by soil swelling. *Geophys. Res. Lett.* **45**, 1888–1896  
286 (2018).
- 287 30. Baum, R. L. & Johnson, A. M. Steady movement of landslides in fine-grained soils: A model  
288 for sliding over an irregular slip surface. *US Geol. Surv. Bull.* 1842 (US Geological Survey,  
289 1993)

290



291  
 292 **Figure 1. Map of the Slumgullion landslide.** **a**, Landslide landscape. Red and blue boxes show  
 293 swaths from Sentinel-1 ascending (T49) and descending (T56) tracks, respectively. White box  
 294 shows UAVSAR swaths. Black and gray lines outline the active and inactive landslides. White  
 295 diamonds show the locations of three extensometers. Structural zones and kinematic elements  
 296 are labeled<sup>8-9, 14</sup>. Red lines show updated boundaries from this study, and dashed lines are  
 297 tentative. **b&c**, Sentinel-1 line-of-sight (LOS) displacements positive towards the satellite,  
 298 superimposed on the shaded relief LiDAR DEM. Three symbols (o\|x\|+) show targets with time-  
 299 series plots in Fig. 4a.  
 300

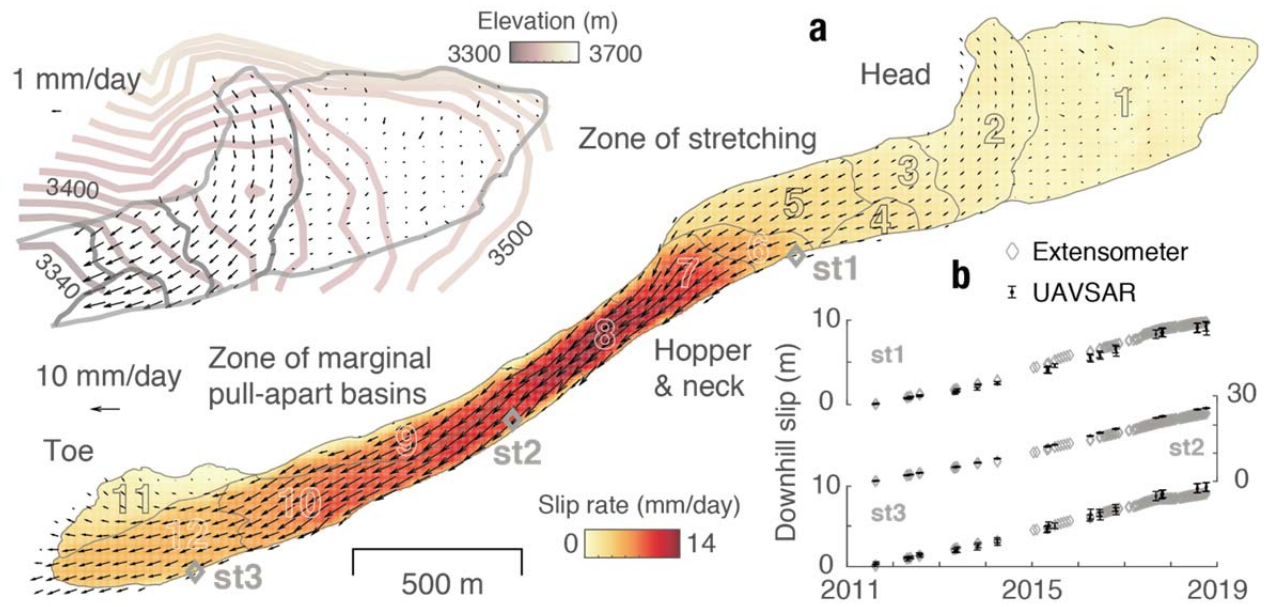


302

303 **Figure 2. Surface and subsurface landslide kinematics.** **a**, Transverse profiles selected every  
 304 50 m and differentiated by colors; the dashed gray line delineates the central axis. **b**,  
 305 Longitudinal surface velocity from hybrid InSAR/POT analysis of UAVSAR data; colored lines  
 306 represent 1-km-long profiles in **a**; shaded sections are within the lateral margins determined by  
 307 the velocity profiles. **c**, Example of the inferred channel geometry and slip rates at the surface  
 308 (compared with SAR results) and subsurface. Geometric steepness and bed tilt are indicated by  
 309 white and black dashed lines, respectively. **d**, 3D view of landslide surface and the inferred basal  
 310 morphology. **e**, Changing characteristic geometric parameters along the landslide. Symbols are  
 311 the individual results for each profile with fitting lines in corresponding colors also used for y-  
 312 axis labels.

313



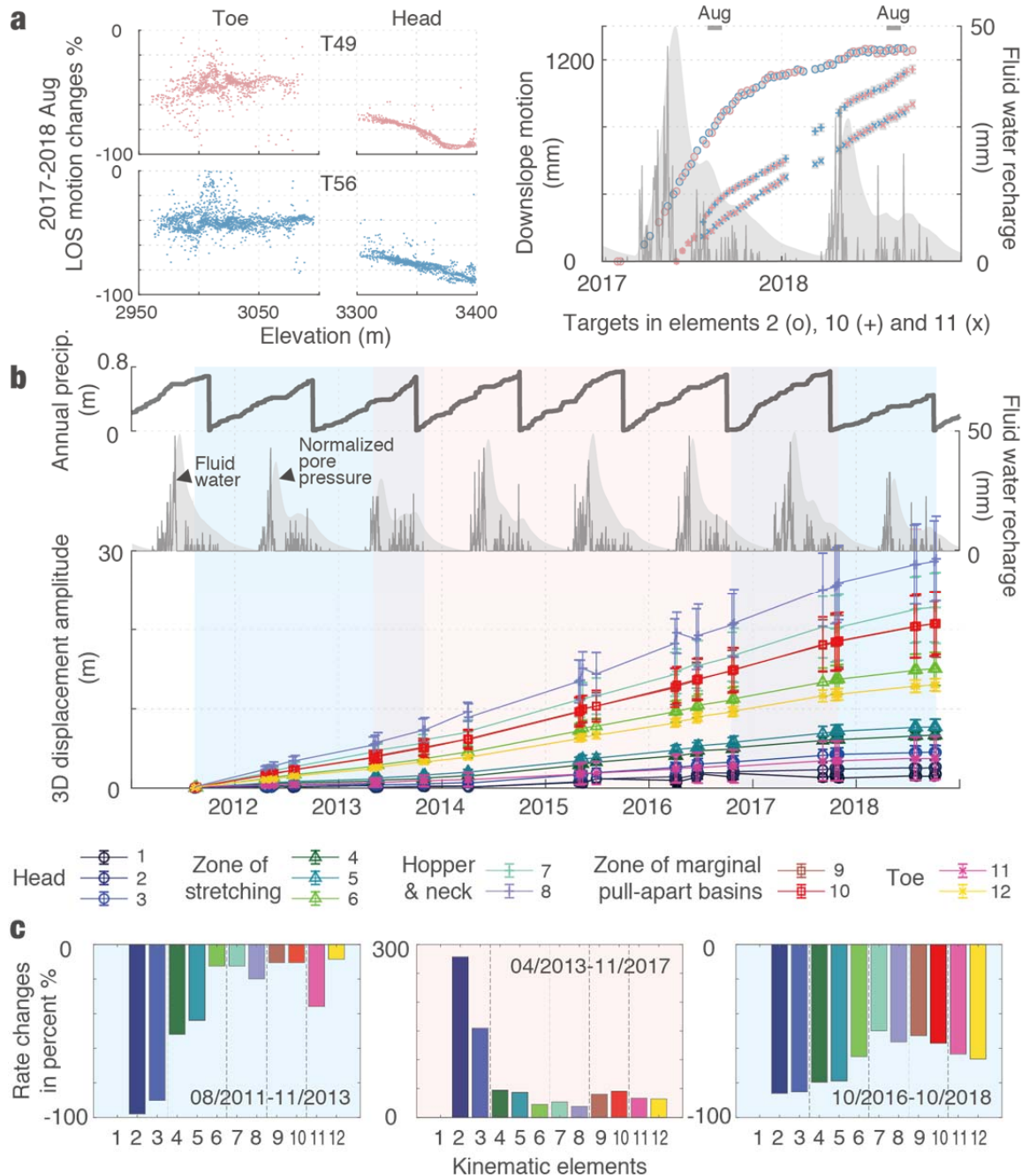


314

315 **Figure 3. Landslide spatial dynamics.** a, Horizontal slip vectors derived from 2011-2018  
 316 UAVSAR data with net 3D velocities in color. Inset close-up view of the head also shows  
 317 elevation contours. b, Comparisons between UAVSAR time series and data from three  
 318 extensometers (locations as in a).

319





320

321 **Figure 4. Multi-annual landslide motions.** a, Results from Sentinel-1 ascending (red) and  
 322 descending (blue) data. The left panel shows the line-of-sight velocity changes between August  
 323 2017 and 2018 over the head and toe, plotted against the elevation. The right panel shows the  
 324 downslope motion of selected targets (locations in Fig. 1). b, 3D displacement amplitude for  
 325 each kinematic element in indicated colors from UAVSAR hybrid InSAR-POT analysis. Blue  
 326 and red shades on the background show the time periods of observed deceleration and

327 acceleration, respectively, consistent with the meteorological data. The annual precipitation  
328 observations, the estimated water recharge at the surface, and the normalized pore pressure at 20-  
329 m depth are shown in gray thick, thin lines and shades, respectively. **c**, Multi-year rate changes in  
330 three respective periods for the kinematic elements.

331

332 **Acknowledgments:**

333 We thank the UAVSAR flight and data processing teams for acquiring the data and processing  
334 the SLC stacks. We thank all the data providers – UAVSAR, Sentinel-1, LiDAR DEM,  
335 meteorological data can be freely downloaded from the NASA/JPL, Copernicus Open Access  
336 Hub and Alaska Satellite Facility, OpenTopography, and U.S. Natural Resources Conservation  
337 Service, respectively. This research was sponsored by the NASA Earth Surface and Interior  
338 Geodetic Imaging program. Part of this research was performed at the Jet Propulsion Laboratory,  
339 California Institute of Technology under contract with NASA. Mention of trade names or  
340 commercial products is not an endorsement or recommendation for use by the U.S. Government.